CHEMISTRY OF MATERIALS

Article

pubs.acs.org/cm

# Polymorph Engineering of $TiO_2$: Demonstrating How Absolute Reference Potentials Are Determined by Local Coordination

John Buckeridge,*[,†] Keith T. Butler,[‡] C. Richard A. Catlow,[†] Andrew J. Logsdail,[†] David O. Scanlon,[†,§] Stephen A. Shevlin,[†] Scott M. Woodley,[†] Alexey A. Sokol,[†] and Aron Walsh[‡]

[†]Kathleen Lonsdale Materials Chemistry, Department of Chemistry, University College London, 20 Gordon Street, London WC1H 0AJ, United Kingdom

[‡]Centre for Sustainable Chemical Technologies and Department of Chemistry, University of Bath, Claverton Down, Bath BA2 7AY, United Kingdom

[§]Diamond Light Source Ltd., Diamond House, Harwell Science and Innovation Campus, Didcot, Oxfordshire OX11 0DE, United Kingdom

**ABSTRACT:** We report that the valence and conduction band energies of $TiO_2$ can be tuned over a 4 eV range by varying the local coordination environments of Ti and O. We examine the electronic structure of eight known polymorphs and align their ionization potential and electron affinity relative to an absolute energy reference, using an accurate multiscale quantum-chemical approach. For applications in photocatalysis, we identify the optimal combination of phases to enhance activity in the visible spectrum. The results provide a coherent explanation for a wide range of phenomena, including the performance of $TiO_2$ as an anode material for Li-ion batteries, allow us to pinpoint hollandite $TiO_2$ as a new candidate transparent conducting oxide, and serve as a guide to improving the efficiency of photo-electrochemical water splitting through polymorph engineering of $TiO_2$.

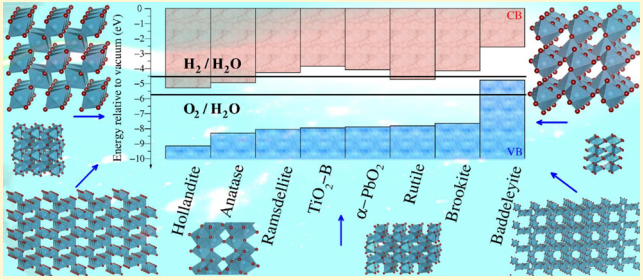


## INTRODUCTION

Optical and electronic engineering of metal oxides for a range of technological applications has led to the study of increasingly complex multicomponent systems, recently including mixed-anion solid solutions for modification of the valence band energy.[1−7] The inherent chemical and structural disorder of multicomponent systems results in variation in materials properties and performance and provides a major challenge for scaling up toward application on a commercial scale. An alternative approach is to start with fewer chemical components and control the *structure* rather than the *composition*, which is the topic addressed in this study.

Most metal oxides can adopt a range of crystal structures depending on the preparation and treatment conditions. In addition to known polymorphs in the equilibrium phase diagram, the development of non-equilibrium growth techniques, such as atomic-layer deposition, provides an opportunity to exploit hitherto unknown metastable structural configurations.[8]

The importance of local structure in determining the observable properties of a material has been discussed since the advent of crystallography.[9] In the context of ionic solids, a key descriptor is the Madelung potential of each crystallographic site, which is determined by a summation to infinity over the ionic charges of the surrounding ions.[10] Knowledge of the variations in the local electrostatic potential proved key to the development of theories of work functions,[11] to defect chemistry including ionic conductivity,[12] and even, for example, to the understanding of the nature of hole pairing in high-temperature superconductors.[13]

Since the discovery in 1972 by Fujishima and Honda[14] of the ability of $TiO_2$ to split water using sunlight, there has been extensive research into improving the efficiency of this process. It has been found that samples containing a mixture of the most abundant phases of $TiO_2$, anatase and rutile, outperform pure phase samples.[15] We have recently explained this behavior by the variation in the electrostatic potential of Ti and O in the two polymorphs, which drives changes in the ionization potential and electron affinity (work function) of the materials.[16] The idea of mixing other known polymorphs of $TiO_2$, including brookite and $TiO_2$-B, is a natural extension of this concept, but has to date not been explored.

A key requirement for the water-splitting process is that the electronic energy bands of the photoelectrode are aligned with respect to the redox potentials of water. In electronic structure calculations, under periodic boundary conditions, there is no absolute reference potential.[17] The absence of a well-defined vacuum level hinders prediction of the suitability of novel materials for photoelectrochemical, or indeed photovoltaic or other optoelectronic, applications. To overcome this problem,

Received: January 19, 2015
Revised: May 1, 2015
Published: May 1, 2015





DOI: 10.1021/acs.chemmater.5b00230
*Chem. Mater.* 2015, 27, 3844−3851

we have developed a multiregion, quantum mechanical/molecular mechanical (QM/MM) solid-state embedding procedure. The embedding procedure exploits the "tinfoil" boundary condition in the three-dimensional electrostatic (Ewald) summation to provide an absolute reference. This approach advantageously treats all possible charge (oxidation) states of the defect (e.g., created by electron addition or removal) within the same reference frame.

In this work, we consider all four naturally occurring $TiO_2$ phases, as well as four phases that have been sythesized experimentally. We relate the variations in ionization potential and electron affinity of each polymorph to the differences in crystal structure, and in particular to the local coordination environments and medium-range order of oxygen and titanium. To complement our embedding procedure, density functional theory (DFT) within periodic boundary conditions is used to calculate the full electronic band structure of each material and to construct a complete band alignment scheme for the binary $TiO_2$ system. The scheme developed here should provide a solid foundation for future studies and optimization of titania based materials and devices but has a relevance to a wider range of metal oxide applications.

## COMPUTATIONAL DETAILS

We utilize two approaches to determine the electronic energy bands of each polymorph of $TiO_2$ relative to the vacuum.

**Solid-State Embedding.** We employ a hybrid QM/MM embedded cluster approach, as implemented in the ChemShell code,[64,65] which provides direct access to the vacuum level without any surface present. The method for calculating $I$ consists of modeling a charged defect (in this case a hole at the top of the valence band in bulk) within a cluster of about 80 atoms treated at a QM level of theory, which is embedded in a larger cluster of about 10,000 atoms treated at an MM level of theory. The MM cluster is modeled using a polarizable shell interatomic force field[66] that accurately reproduces the high-frequency dielectric tensor of bulk[12,16] so that it provides the correct polarization response of the surrounding infinite solid to the charged defect in the QM region. In this way the defect is treated at the dilute limit.[67]

$I$ is determined using a ΔSCF (self-consistent field) approach, i.e., by calculating the energy difference between the system in the neutral and positive charge states. The accuracy of this approach is well-established.[16,52,68−72]

*Cluster Size.* For each phase, a spherical cut of the bulk material of radius 30 Å was taken. This sphere was then surrounded by point charges, the charges of which were fitted to reproduce the Madelung potential of the infinite system within the central region of the sphere (with a tolerance of $10^{-6}$ V). The sphere is divided into a QM region at the center, surrounded by an interface region, then an active MM region, and then a 15 Å wide frozen MM region (see ref 67 for more details). The QM region does not need to be stoichiometric nor charge neutral owing to the boundary conditions of the cluster model. We used different QM region sizes in order to test for convergence. For rutile, anatase, brookite, $TiO_2$-B, $\alpha$-$PbO_2$, baddeleyite, hollandite, and ramsdellite the smaller QM cluster size consisted of 55, 47, 51, 47, 69, 91, 43, and 43 atoms, respectively; the larger QM cluster size consisted of 71, 79, 71, 93, 89, 102, 73, and 79 atoms, respectively. The resulting ionization potentials were converged within approximately 2%.

*QM Region.* QM calculations were done using the Gamess-UK[73] code. A triple-$\zeta$ valence plus polarization Gaussian basis set was used for Ti and O ions, with a 10 core electron effective core potential (ECP) used in modeling Ti atoms.[74,75] Electron exchange and correlation were treated at the level of hybrid meta-GGA, as parametrized in the BB1k formalism,[76] which gives a highly accurate description of electron localization, atomization energies, and thermochemistry.

*MM Region.* MM calculations were performed using the GULP code.[77] The shell polarizable interatomic force field we have used to treat the MM region is a modification of a force field model previously derived to treat $SrTiO_3$,[12,16] which was based on the Born model of ionic solids.[78] The model is designed to reproduce the high-frequency dielectric properties of $TiO_2$, meaning that it has been employed to relax electronic degrees of freedom only. We simulate ion−ion interactions as two-body interactions using a Coulomb sum:

$$U_{ij}^{\text{Coulomb}} = k\frac{q_i q_j}{r_{ij}} \tag{1}$$

where $U_{ij}$ is the energy of interaction, $r_{ij}$ is the separation between ions $i$ and $j$, $q_i$ is the charge on ion $i$, and $k$ is a dimensional unit constant; and using a Buckingham potential, including a dispersion term, of the form

$$U_{ij}^{\text{Buck}} = A\,\exp(r_{ij}/\rho) - \frac{C}{r_{ij}^{\,6}} \tag{2}$$

where the parameters $A$, $\rho$, and $C$ depend on species $i$ and $j$.

The polarizability of the ions is taken into account using the shell model of Dick and Overhauser,[66] where each ion is separated into a core and shell, with the massless shell (charge $Y$) connected to the core by a spring. The total charge of the core−shell equals the formal charge of the ion. The energy is given by

$$U_{\text{c-s}} = \frac{1}{2}K r_{\text{c-s}}^{\,2} + \frac{1}{24}K_4 r_{\text{c-s}}^{\,4} \tag{3}$$

where $K$ and $K_4$ are the spring constants and $r_{\text{c-s}}$ is the distance between the core and shell. The parameters used are given in Table 1.

**Table 1. Interatomic Potential Parameters for Bulk $TiO_2$, Including Shell Polarization on Ti and O Ions ($e$ Is the Electron Charge)**

| Buckingham | $A$ (eV) | $\rho$ (Å) | $C$ (eV Å$^{-6}$) |
|---|---|---|---|
| O shell — O shell | 22764.3 | 0.15 | 43.0 |
| O shell — Ti shell | 835.0 | 0.38 | 9.6 |
| shell | $K$ (eV Å$^{-2}$) | $Y(e)$ | $K_4$ (eV Å$^{-4}$) |
| Ti core — Ti shell | 981.4 | −1.00 | 50000 |
| O core — O shell | 11.7 | −2.39 | 50000 |

This force field model was also used in calculating the Madelung potentials and defect energies within the Mott−Littleton[11] approach. We note that, in using a common reference, i.e., the vacuum level, we are able to compare directly calculated ionization potentials across the different polymorphs.

*Interface Region.* To treat the interface between the QM and MM regions, a specially designed local ECP was placed on Ti sites located within a range of 5 Å, from the edge of the QM region.[16] The ECP $U_p(r)$ has the following form:

$$r^2 U_p(r) = A_1 r\,\exp(-Z_1 r^2) \tag{4}$$

where the parameters $A_1$ and $Z_1$ were fitted in order to minimize the gradients on the ions in the QM and interface region and the spread of deep core levels in the energy spectrum. The parameters are (in atomic units) $A_1 = 0.935$ and $Z_1 = 0.356$.

**Periodic Models of the Ideal Solid.** The band gap of each polymorph was determined using plane-wave DFT, treating electron exchange and correlation with the screened hybrid HSE06 functional.[79] We use plane-wave DFT, as calculating the electron affinity accurately would require a bigger cluster model and basis sets that are much too large for current computing resources. When calculating $I$ using the ΔSCF approach, the BB1k functional accounts for the self-interaction error,[16] while when calculating $E_g$, the HSE06 functional describes well the periodic solid, and indeed is known to reproduce accurately the band gaps of rutile and anatase.[61]



DOI: 10.1021/acs.chemmater.5b00230
Chem. Mater. 2015, 27, 3844−3851

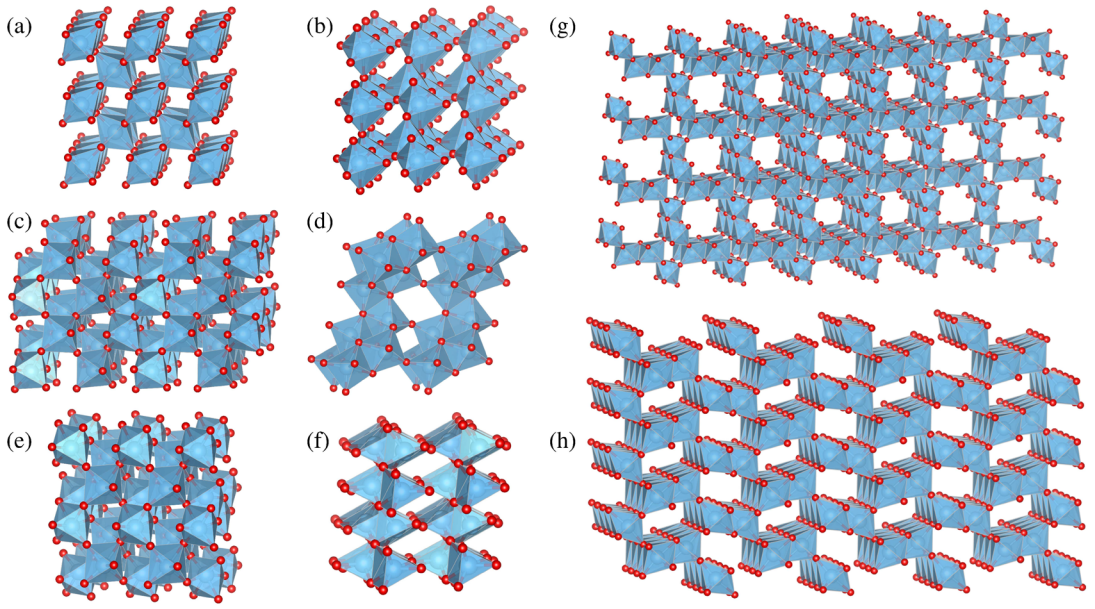


**Figure 1.** Different phases of $TiO_2$ considered in this study: (a) rutile, (b) anatase, (c) brookite, (d) $TiO_2$-B, (e) $\alpha$-$PbO_2$, (f) baddeleyite, (g) hollandite, and (h) ramsdellite (see text for references and space groups). Polyhedra consisting of Ti atoms and nearest-neighbor O are represented in blue. O atoms are represented by red spheres.

The plane-wave DFT calculations were performed using the VASP code,[80−83] with the projector augmented wave approach[84] used to describe the interaction between the core (Ti:[Ar], O:[He]) and valence electrons. A plane-wave cutoff of 500 eV was used in each case, and for the rutile, anatase, brookite, $TiO_2$-B, $\alpha$-$PbO_2$, baddeleyite, hollandite, and ramsdellite phases we used a $4 \times 4 \times 6$, $4 \times 4 \times 4$, $2 \times 4 \times 4$, $4 \times 4 \times 4$, $4 \times 4 \times 4$, $4 \times 4 \times 4$, $3 \times 3 \times 3$, and $2 \times 6 \times 4$ special $k$-points mesh centered at the $\Gamma$ point, respectively. These settings provided total energy convergence within $10^{-4}$ eV/atom. The band gap calculations were performed using unit cells derived from the experimental lattice parameters, with the ions kept at their experimentally determined positions.

## RESULTS AND DISCUSSION

**Polymorphs of $TiO_2$.** The crystal structures of the eight polymorphs considered here are shown in Figure 1. In all of our calculations, we fix the ionic coordinates at the experimentally determined values and relax the electronic degrees of freedom. Performing the calculations in this manner means that a comparison of the total energies of the phases is of limited value; nevertheless the calculated energies are sufficiently close (within a range of 0.03 eV per atom) to be consistent with the observed polymorphism. The naturally occurring phases considered are as follows (space groups in parentheses): rutile ($P4/mnm$),[18] anatase ($I4_1/amd$),[19] brookite ($Pbca$),[20] and $TiO_2$-B ($C2/m$).[21] The synthetic polymorphs include the high-pressure phases $\alpha$-$PbO_2$ ($Pbcn$)[22] and baddeleyite ($P2_1/c$)[23] (in the limit of ambient pressure) and the nanoporous phases hollandite ($I4/m$)[24] and ramsdellite ($Pbnm$).[25]

Each polymorph typically consists of ordered arrays of $TiO_6$ distorted octahedra, with three-coordinated oxygens, apart from the baddeleyite phase which has seven-coordinated Ti and a mix of two- and four-coordinated O and the $TiO_2$-B phase which has two-, three-, and four-coordinated O. The phases differ in the order, distortion, and connectivity of the polyhedra.[26,28] Relevant structural data can be gleaned from publicly accessible databases; e.g., see ref 27.

**Absolute Electronic Energy Levels.** We report the calculated ionization potential ($I$), determined using the hybrid QM/MM approach, the energy band gap ($E_g$), determined using plane-wave DFT, and the derived electron affinity ($A$, where $A = I - E_g$) of each polymorph in Table 2 and depict the resulting band alignment, relative to an absolute vacuum potential in Figure 2. These values are compared to the position of the redox potentials of water obtained from the standard hydrogen electrode potential ($E(H^+/H_2)$ = 4.44 V relative to vacuum at room temperature[29]) and the water-splitting free energy of 1.23 eV.[30−32] For comparison, we show in Table 2 experimentally determined values of $E_g$ where available. For rutile and anatase, the band gap values are from low-temperature and ambient-pressure measurements,[33,34] while for the less well studied brookite phase we show the range of experimental values that have been reported.[35]

Variation in the ionization potential, electron affinity, and band gap of 4.39 eV, 2.73 eV, and 1.91 eV, respectively, is calculated across the eight polymorphs. The baddeleyite phase exhibits an anomalous behavior, with an exceptionally high

**Table 2. Calculated Ionization Potential ($I$), Determined Using a ΔSCF Approach within a QM/MM Embedded Cluster Model, Energy Band Gap ($E_g$), Determined Using Plane-Wave DFT with a Hybrid Functional, and Derived Electron Affinity ($A = I - E_g$) of Each of the $TiO_2$ Polymorphs[a]**

| polymorph | $I$ (eV) | $E_g$ (eV) | $A$ (eV) | exptl $E_g$ (eV) |
|---|---|---|---|---|
| rutile | 7.83 | 3.10 | 4.73 | 3.031[b] |
| anatase | 8.30 | 3.36 | 4.94 | 3.23[c] |
| brookite | 7.66 | 3.51 | 4.15 | 3.1−3.4[d] |
| $TiO_2$-B | 7.97 | 4.11 | 3.86 | |
| $\alpha$-$PbO_2$ | 7.89 | 3.81 | 4.08 | |
| baddeleyite | 4.77 | 2.20 | 2.57 | |
| hollandite | 9.16 | 3.86 | 5.30 | |
| ramsdellite | 8.05 | 3.78 | 4.27 | |

[a]Experimental values of $E_g$ are given for comparison where available. [b]Reference 33. [c]Reference 34. [d]Reference 35.



DOI: 10.1021/acs.chemmater.5b00230
Chem. Mater. 2015, 27, 3844−3851

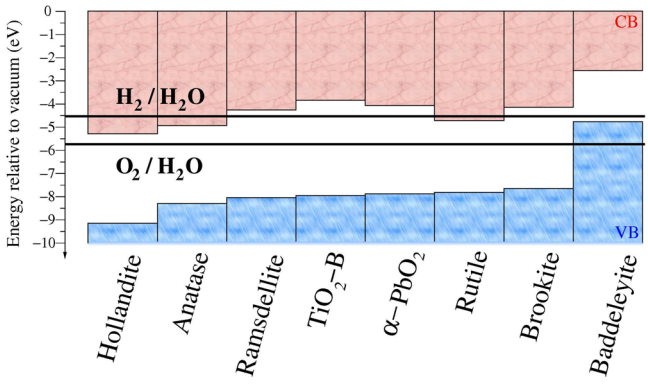


**Figure 2.** Calculated valence band (VB) and conduction band (CB) positions relative to the vacuum level for the various $TiO_2$ polymorphs considered, shown in comparison with the $H_2$ and $O_2$ redox potentials.

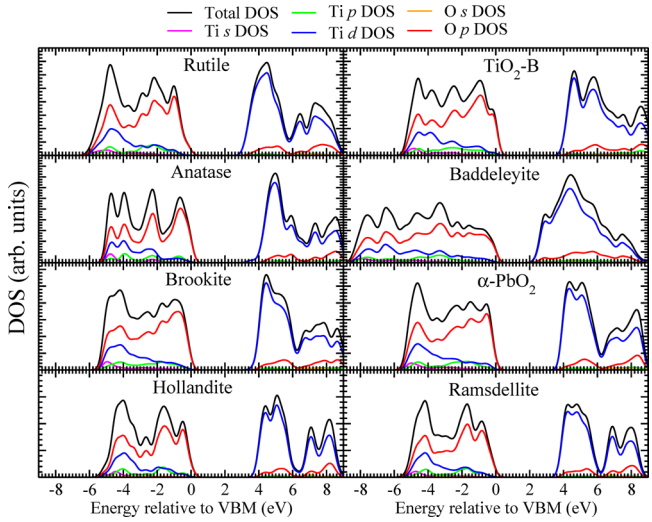


**Figure 3.** Calculated electronic density of states (DOS) and partial DOS (including contributions from s, p, and d orbitals) of the $TiO_2$ polymorphs as a function of energy relative to the valence band maximum (VBM).

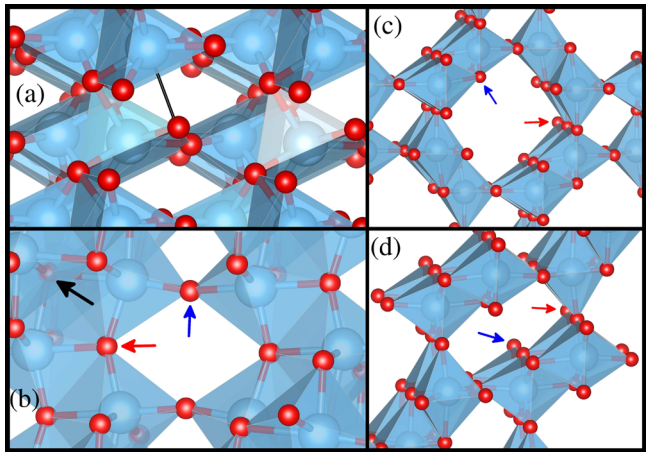


**Figure 4.** More detailed view of the local structure in (a) the baddeleyite phase, where the bridging bond between a two-coordinated oxygen and the titanium at the center of a second-nearest-neighbor trigonal prism is shown in black; (b) the $TiO_2$-B phase, where two-, three-, and four-coordinated oxygens are indicated by blue, red, and black arrows, respectively; (c) the hollandite and (d) ramsdellite phases, indicating a trigonal planar coordination site (red arrow) and a trigonal pyramidal coordination site (blue arrow).

position of the valence band (low ionization potential of 4.77 eV) and a much lower electron affinity (work function of 2.57 eV), which combine to give a significantly reduced band gap of 2.2 eV. From the other phases, the maximum value of $I$ is found for the hollandite phase (9.16 eV), while the minimum value is obtained for brookite (7.66 eV).

The baddeleyite phase is different from the others in terms of its coordination of Ti (seven as opposed to six) and has a mix of two- and four-coordinated O, which only the $TiO_2$-B phase shares. The Madelung potential ($V_M$) at each ionic site has been calculated, taking into account the intrinsic electron polarization of each polymorph. We find that the two differently coordinated O sites in baddeleyite have quite different values of $V_M$: 22.5 and 29.9 V for two- and four-coordinated ions, respectively. Lower potentials indicate higher electronic energies at anionic sites. The low Madelung potential at the low-coordination site correlates well with the dramatic offset in the values of the ionization potential between baddeleyite and the other phases. Indeed, on comparing the relevant $V_M$ we find a 3.6 eV offset between baddeleyite and brookite, in agreement with the trend we observe using our QM/MM approach.

To provide further support to the preceding analysis, we employ the approach of Mott and Littleton,[11,36] which includes dynamic polarization effects of the extended crystal. Here, the ionization process is simulated as the formation of a hole on an oxygen site. In $TiO_2$, the valence band is formed predominately from overlap of oxygen 2p-like states (see the electronic density of states in Figure 3) as seen universally in other ab initio electronic structure calculations[37] and from photoemission spectroscopy.[38] Following the self-consistent Mott–Littleton procedure, which accounts for electronic relaxation in response to hole formation, we calculated the ionization potentials for the titania polymorphs in close agreement with the *ab initio* QM/MM data. We have obtained in fact an improvement on the results based on the Madelung potentials. Crucially, comparing the quasi-particle hole energy between the brookite and baddeleyite phases (cf. 3.1 eV vs 2.9 eV from the Mott–Littleton and QM/MM approaches, respectively), we observe the same dramatic offset as quantum-chemical simulations.

To rationalize the difference in behavior, we now investigate the local environment of the polymorphs in further detail. In baddeleyite, the titanium coordination can be viewed as trigonal prismatic (6-fold-coordinate), where the prisms form an edge-sharing bilayer network (see Figure 4a). Two oxygen ions, defining one of the prism side edges, bridge between adjacent bilayers and connect two nearest prisms within a layer. At the same time, a third longer coordinate bond is formed between each of these oxygens and a second-nearest-neighbor prism (giving rise to the seventh Ti–O bond). Thus baddeleyite stands out in its properties, which are directly correlated to the local atomic structure. Indeed, all other polymorphs of $TiO_2$ consist of edge- and corner-sharing octahedra, rather than prisms, and the only other example of a two-coordinated oxygen is the linear bridge between adjacent octahedral bilayers found in $TiO_2$-B.

A similar set of arguments helps explain the behavior of band edges in the other polymorphs. In the first instance, we consider the hollandite phase, which has the largest $I$ of all of the polymorphs. Analyzing the local coordination of oxygen ions (see Figure 4c,d), we observe two basic environments


DOI: 10.1021/acs.chemmater.5b00230
*Chem. Mater.* 2015, 27, 3844–3851

which are shared by both nanoporous phases, ramsdellite and hollandite: in one the ion is surrounded by three Ti sites in a slightly distorted planar trigonal configuration; in the other the oxygen ion has a trigonal pyramidal coordination. The former configuration is common to many $TiO_2$ polymorphs including the three most common: rutile, anatase, and brookite. We find that, in the perfect crystal, the Madelung potential on the trigonal pyramidal site, in comparison with the planar site, is significantly less stable (by 0.9 V). The order, however, is reversed when we use the Mott−Littleton approach (allowing all electronic degrees of freedom to relax), due to the strong stabilization of the trigonal pyramidal sites by the Madelung field—a local polarization effect. Furthermore, hollandite has a particularly porous structure, where the Coulomb interaction between oxygen ions across the channels (or pores) is much weaker than in its denser counterpart polymorphs, including even the other nanoporous structure (ramsdellite). This structural motif could be utilized in future polymorph engineering studies aimed at obtaining novel materials with a deep position of the valence band.

For the $TiO_2$-B phase, which has two-, three-, and four-coordinated oxygen-ion sites (see Figure 4b), we calculate the least stable $V_M$ at the two-coordinated sites, with a potential offset of 2.3 V. $V_M$ at the three- and four-coordinated sites is in fact similar in value to that in other octahedral polymorphs. From our quantum-chemical calculations (see Figure 2), we determine the valence band of this phase to lie close to that of ramsdellite, $\alpha$-$PbO_2$, and rutile, in contrast to our molecular mechanical result (which would place its valence band ∼2 eV higher). The origin of this discrepancy lies in the overestimation of the polarizability of the two-coordinated sites in this material. Using the Mott−Littleton approach to treat the polarization more accurately, while appropriately constraining the electron density on the two-coordinated sites and accounting for differences in the short-range ion−ion interaction, restores the generally very good correlation between the quantum mechanical and molecular mechanical methods, with the discrepancy reducing to ∼0.1 eV.

**Applications.** *Photoelectrochemical Water Splitting.* The type-II band alignment predicted for the rutile−anatase mixture has two advantages for efficient water splitting using visible light. First, on excitation, it is favorable for electrons to flow from rutile to anatase, as the CBM of anatase is below that of rutile, and for holes to flow in the opposite direction due to the relative position of the VBMs, which leads to efficient electron−hole separation. Second, the effective band gap of the mixture is lower than that of the constituent polymorphs, leading to improved visible light absorption. In water-splitting applications, the most efficient use of available light sources is sought, which is solar radiation in the visible range, hence the desire for materials absorbing in this range. We note that UV sources can also be used in industrial or laboratory settings where high conversion rates can be achieved.

In a recent experiment,[39] it was found that using the $\alpha$-$PbO_2$ polymorph resulted in an improvement in $H_2$ production from water over using rutile or anatase. We can now explain this observation by comparing the electron affinity of the three phases. We find that the conduction band of the $\alpha$-$PbO_2$ phase lies 0.37 eV above the reduction potential of water, in contrast to rutile and anatase, where the bulk level is *below* the redox potential. We note that when the CBM lies below the $H^+/H_2$ redox potential, it seems that water splitting will not occur under zero bias; instead a voltage would need to be applied. However, by careful engineering of suitable surfaces or interfaces one can achieve a further offset of the CBM, which raises it above the redox potential.

A favorable conduction band position is also found in the brookite phase. Indeed, it has been found experimentally that thin film samples of brookite $TiO_2$ outperform anatase and rutile.[35,40] We note that the improvement in ref 40 was attributed to increased absorption in the visible spectrum due to the presence of defects, which may also play a role in improving performance; but the more favorable band alignment will provide a greater thermodynamic driving force for the reduction reaction.

It is worth also commenting that using baddeleyite, given the calculated valence band position relative to the water oxidation potential, it should be possible to dampen the $H_2O$ oxidation reaction, which could lower the rate of hydroxyl radical formation.

As mentioned above, two factors in the band alignment of rutile and anatase contribute to the enhanced performance of the mixture: increased efficiency of electron−hole separation and a reduction in the effective band gap. From Figure 2 we can conclude that an enhancement of both of these factors should be possible by mixing anatase with either the brookite, $TiO_2$-B, or $\alpha$-$PbO_2$ polymporphs. We therefore predict that improved performance can be achieved using mixtures of anatase with these three polymorphs. To our knowledge, water splitting using such mixtures has not yet been attempted. We note, however, that anatase/$TiO_2$-B mixed samples have been used for photocatalytic sulforhodamine B degradation[41] and anatase/brookite mixed samples have been used for photocatalytic methylene blue degradation.[42] In both cases, it was found that the mixed-phase samples outperformed the pure phases, which would follow from our calculated band alignment and supports our prediction of improved water-splitting performance.

Furthermore, a recent study[43] found that mixed anatase/brookite samples showed reduced photoluminescence in comparison to the pure phases, indicating increased charge separation. Again, this result would follow from our calculated band alignment.

While producing mixed-phase samples may pose synthetic challenges, a recent procedure reported in ref 44 may be ideal for testing our predictions. The approach has been used to form epitaxially sharp anatase/$TiO_2$-B interfaces, with a minimum of stacking faults or dislocation defects, but could also be applied to the other polymorphs discussed here. Reference 44 also provided results from DFT calculations, which confirmed the spatially separated valence and conduction band edges by analyzing the electron density. They found that the valence states were localized in the $TiO_2$-B layer and the conduction states in the anatase layer. Their results, obtained using a different electronic structure approach, agree well with our calculated $TiO_2$-B/anatase band alignment.

*Electrochemical Energy Storage.* Our calculated electronic band alignment reveals an important factor that contributes to $TiO_2$-B outperforming both anatase and rutile as an anode for lithium-ion batteries.[45]

The conduction band position of $TiO_2$-B is closer to the vacuum level than that of both anatase and rutile. The electronic chemical potential of $TiO_2$-B is higher than that of the other two phases; therefore its open-cell voltage is also higher. Importantly, its electrochemical potential remains below the redox potential of common liquid electrolytes.[46,47] The open-cell voltages for batteries using $TiO_2$-B, anatase, and rutile


DOI: 10.1021/acs.chemmater.5b00230
Chem. Mater. 2015, 27, 3844−3851

are 1.6,[45] 1.55,[48] and 1.4 V,[49] respectively. If the baddeleyite phase could be stabilized in a form suitable for a battery anode, it could provide a step change in performance.

*Optoelectronics.* The calculated electron affinity of hollandite is greater than that of all of the other polymorphs. Following the doping limit rules, materials with a greater electron affinity are more easily n-type doped.[50−52]

Anatase $TiO_2$ is an effective transparent conducting oxide (TCO) when donor doped with Nb or F.[53,54] The higher work function of hollandite, together with its large fundamental band gap of 3.86 eV, indicate that it will be a superior n-type TCO than anatase and could be ideal for both conventional *and* ultraviolet TCO applications. The latter is of particular interest for improving the performance of photovoltaic devices as well as short-wavelength light emitting diodes.[55]

**Beyond Bulk Energy Levels.** A close look at the literature, including photoemission, electrochemical, and thermionic measurements, will reveal a great range in the reported values of work function, ionization potential, and electron affinity of $TiO_2$.[56] To consider this variation, one must take into account factors that are overlooked by bulk band alignments alone.

Surface termination and morphology,[57−59] as well as features such as charge carrier lifetimes, polaronic trapping, and charge migration to the surface, play an important role in photocatalysis and photoelectrochemistry.[15,60−63] These effects should be taken into consideration when explaining the observable properties of all $TiO_2$ polymorphs.

Despite these factors, bulk band alignment will provide the fundamental energetics upon which a theory of electron and hole dynamics can be built and constitutes an important initial approximation.

## ■ CONCLUSIONS

We have calculated the conduction and valence band edge energies relative to the vacuum for eight different polymorphs of $TiO_2$, using a multiscale approach. From our results we determined the titania bulk electronic band alignment, which has been rationalized as an effect of local coordination. The electronic energy levels of each phase are evidently correlated with the Madelung potentials of the constituent ions.

The proposed scheme has been employed to shed light on a number of key technological applications of this class of material. By comparing the band positions on an absolute energy scale, we can explain observed improvements in water-splitting performance by the $\alpha$-$PbO_2$ and brookite phases and by mixed-phase samples. We also give an explanation for the improved performance of $TiO_2$-B as an anode in Li-ion batteries and suggest that hollandite $TiO_2$ should be a superior transparent conducting oxide. Our results serve as a general guide to engineering local structure in order to maximize function in the solid state.

## ■ AUTHOR INFORMATION

### Corresponding Author

*E-mail: j.buckeridge@ucl.ac.uk.

### Notes

The authors declare no competing financial interest.

## ■ ACKNOWLEDGMENTS

We acknowledge funding from EPSRC Grants EP/D504872, EP/I01330X/1, and EP/K016288/1. The simulations made use of the UCL Legion High Performance Computing Facility, the IRIDIS cluster provided by the EPSRC funded Centre for Innovation (Grants EP/K000144/1 and EP/K000136/1), and the ARCHER supercomputer through membership of the U.K.'s HPC Materials Chemistry Consortium (EPSRC Grant EP/L000202). J.B. thanks S.-H. Wei for useful discussions. A.W. and D.O.S. acknowledge membership of the Materials Design Network. A.J.L. thanks the Ramsay Memorial Trust for providing a fellowship.

## ■ REFERENCES

(1) Maeda, K.; Domen, K. Photocatalytic water splitting: Recent progress and future challenges. *J. Phys. Chem. Lett.* **2010**, *1*, 2655−2661.

(2) Chen, S.; Gong, X. G.; Walsh, A.; Wei, S.-H. Crystal and electronic band structure of $Cu_2ZnSnX_4$ (X = S and Se) photovoltaic absorbers: First-principles insights. *Appl. Phys. Lett.* **2009**, *94*, No. 041903.

(3) Hiramatsu, H.; Kamiya, T.; Tohei, T.; Ikenaga, E.; Mizoguchi, T.; Ikuhara, Y.; Kobayashi, K.; Hosono, H. Origins of Hole Doping and Relevant Optoelectronic Properties of Wide Gap p-Type Semiconductor, LaCuOSe. *J. Am. Chem. Soc.* **2010**, *132*, 15060−15067.

(4) Zakutayev, A.; Tate, J.; Platt, H. A. S.; Keszler, D. A.; Hein, C.; Mayer, T.; Klein, A.; Jaegermann, W. Electronic properties of BaCuChF (Ch = S,Se,Te) surfaces and BaCuSeF/ZnPc interfaces. *J. Appl. Phys.* **2010**, *107*, No. 103713.

(5) Green, D. C.; Glatzel, S.; Collins, A. M.; Patil, A. J.; Hall, S. R. A New General Synthetic Strategy for Phase-Pure Complex Functional Materials. *Adv. Mater.* **2012**, *24*, 5767−5772.

(6) Buckeridge, J.; Scanlon, D. O.; Walsh, A.; Catlow, C. R. A. Automated procedure to determine the thermodynamic stability of a material and the range of chemical potentials necessary for its formation relative to competing phases and compounds. *Comput. Phys. Commun.* **2014**, *185*, 330−338.

(7) Scanlon, D. O.; Buckeridge, J.; Catlow, C. R. A.; Watson, G. W. Understanding doping anomalies in degenerate *p*-type semiconductor LaCuOSe. *J. Mater. Chem. C* **2014**, *2*, 3429−3438.

(8) Alaria, J.; Borisov, P.; Dyer, M. S.; Manning, T. D.; Lepadatu, S.; Cain, M. G.; Mishina, E. D.; Sherstyuk, N. E.; Ilyin, N. A.; Hadermann, J.; Lederman, D.; Claridge, J. B.; Rosseinsky, M. J. Engineered spatial inversion symmetry breaking in an oxide heterostructure built from isosymmetric room-temperature magnetically ordered components. *Chem. Sci.* **2014**, *5*, 1599−1610.

(9) Pauling, L. The principles determining the structure of complex ionic crystals. *J. Am. Chem. Soc.* **1929**, *51*, 1010−1026.

(10) Born, M.; Huang, K. *Dynamical Theory of Crystal Lattices*; Clarendon Press: Oxford, U.K., 1954.

(11) Mott, N. F.; Littleton, M. J. Conduction in polar crystals. I. Electrolytic conduction in solid salts. *Trans. Faraday Soc.* **1938**, *34*, 485−499.

(12) Catlow, C. R. A.; Guo, Z. X.; Miskufova, M.; Shevlin, S. A.; Smith, A. G. H.; Sokol, A. A.; Walsh, A.; Wilson, D. J.; Woodley, S. M. Advances in computational studies of energy materials. *Philos. Trans. R. Soc., A* **2010**, *368*, 3379−3456.

(13) Torrance, J.; Metzger, R. Role of the Madelung energy in hole conductivity in copper oxides: Difference between semiconductors and high-$T_c$ superconductors. *Phys. Rev. Lett.* **1989**, *63*, No. 1515.

(14) Fujishima, A.; Honda, K. Electrochemical Photolysis of Water at a Semiconductor Electrode. *Nature* **1972**, *238*, 37−38.

(15) Li, G.; Gray, K. A. The solid-solid interface: Explaining the high and unique photocatalytic reactivity of $TiO_2$-based nanocomposite materials. *Chem. Phys.* **2007**, *339*, 173−187.

(16) Scanlon, D. O.; Dunnill, C. W.; Buckeridge, J.; Shevlin, S. A.; Logsdail, A. J.; Woodley, S. M.; Catlow, C. R. A.; Powell, M. J.; Palgrave, R. G.; Parkin, I. P.; Watson, G. W.; Keal, T. W.; Sherwood, P.; Walsh, A.; Sokol, A. A. Band alignment of rutile and anatase $TiO_2$ from theory and experiment. *Nat. Mater.* **2013**, *12*, 798−801.



DOI: 10.1021/acs.chemmater.5b00230
*Chem. Mater.* 2015, 27, 3844−3851

(17) Ihm, J.; Zunger, A.; Cohen, M. L. Momentum-space formalism for the total energy of solids. *J. Phys. C: Solid State Phys.* **1979**, *12*, No. 4409.
(18) Baur, W. H. Über die Verfeinerung der Kristallstrukturbestimmung einiger Vertreter des Rutiltyps: $TiO_2$, $SnO_2$, $GeO_2$ und $MgF_2$. *Acta Crystallogr.* **1956**, *9*, 515−520.
(19) Cromer, D. T.; Herrington, K. The Structures of Anatase and Rutile. *J. Am. Chem. Soc.* **1955**, *77*, 4708−4709.
(20) Baur, W. H. Atomabstände und Bindungswinkel im Brookit, $TiO_2$. *Acta Crystallogr.* **1961**, *14*, 214−216.
(21) Feist, T. P.; Davies, P. K. The soft chemical synthesis of $TiO_2$(B) from layered titanates. *J. Solid State Chem.* **1992**, *101*, 275−295.
(22) Filatov, S.; Bendeliani, N.; Albert, B.; Kopf, J.; Dyuzheva, T.; Lityagina, L. Crystalline structure of the $TiO_2$ II high-pressure phase at 293 223, and 133 K according to single-crystal x-ray diffraction data. *Dokl. Phys.* **2007**, *52*, 195−199.
(23) Swamy, V.; Dubrovinsky, L. S.; Dubrovinskaia, N. A.; Langenhorst, F.; Simionovici, A. S.; Drakopoulos, M.; Dmitriev, V.; Weber, H.-P. Size effects on the structure and phase transition behavior of baddeleyite $TiO_2$. *Solid State Commun.* **2005**, *134*, 541−546.
(24) Latroche, M.; Brohan, L.; Marchand, R.; Tournoux, M. New hollandite oxides: $TiO_2$(H) and $K_{0.06}TiO_2$. *J. Solid State Chem.* **1989**, *81*, 78−82.
(25) Akimoto, J.; Gotoh, Y.; Oosawa, Y.; Nonose, N.; Kumagai, T.; Aoki, K.; Takei, H. Topotactic Oxidation of Ramsdellite-Type $Li_{0.5}TiO_2$, a New Polymorph of Titanium Dioxide: $TiO_2$(R). *J. Solid State Chem.* **1994**, *113*, 27−36.
(26) Muscat, J.; Swamy, V.; Harrison, N. M. First-principles calculations of the phase stability of $TiO_2$. *Phys. Rev. B* **2002**, *65*, No. 224112.
(27) *Inorganic Crystal Structure Database*, http://www.fiz-karlsruhe.de/icsd_web.html
(28) De Angelis, F.; Di Valentin, C.; Fantacci, S.; Vittadini, A.; Selloni, A. Theoretical Studies on Anatase and Less Common $TiO_2$ Phases: Bulk, Surfaces, and Nanomaterials. *Chem. Rev.* **2014**, *114*, 9708−9753.
(29) Trasatti, S. The absolute electrode potential: An explanatory note (Recommendations 1986). *J. Electroanal. Chem.* **1986**, *209*, 417−428.
(30) Jaeger, C. D.; Bard, A. J. Spin trapping and electron spin resonance detection of radical intermediates in the photodecomposition of water at titanium dioxide particulate systems. *J. Phys. Chem.* **1979**, *83*, 3146−3152.
(31) Ni, M.; Leung, M. K.; Leung, D. Y.; Sumathy, K. A review and recent developments in photocatalytic water-splitting using for hydrogen production. *Renewable Sustainable Enery Rev.* **2007**, *11*, 401−425.
(32) Kumar, S. G.; Devi, L. G. Review on Modified $TiO_2$ Photocatalysis under UV/Visible Light: Selected Results and Related Mechanisms on Interfacial Charge Carrier Transfer Dynamics. *J. Phys. Chem. A* **2011**, *115*, 13211−13241 (PMID: 21919459).
(33) Amtout, A.; Leonelli, R. Optical properties of rutile near its fundamental band gap. *Phys. Rev. B* **1995**, *51*, 6842−6851.
(34) Kraeutler, B.; Bard, A. J. Heterogeneous photocatalytic decomposition of saturated carboxylic acids on titanium dioxide powder. Decarboxylative route to alkanes. *J. Am. Chem. Soc.* **1978**, *100*, 5985−5992.
(35) Di Paola, A.; Bellardita, M.; Palmisano, L. Brookite, the Least Known $TiO_2$ Photocatalyst. *Catalysts* **2013**, *3*, 36−73.
(36) Catlow, C. R. A.; Mackrodt, W. C. *Computer Simulation of Solids*; Springer: Berlin, 1982.
(37) De Angelis, F.; Di Valentin, C.; Fantacci, S.; Vittadini, A.; Selloni, A. Theoretical Studies on Anatase and Less Common $TiO_2$ Phases: Bulk, Surfaces, and Nanomaterials. *Chem. Rev.* **2014**, *114*, 9708−9753.
(38) Egdell, R.; Eriksen, S.; Flavell, W. Oxygen deficient $SnO_2$(110) and $TiO_2$(110): A comparative study by photoemission. *Solid State Commun.* **1986**, *60*, 835−838.
(39) Murata, H.; Kataoka, Y.; Kawamoto, T.; Tanaka, I.; Taniguchi, T. Photocatalytic activity of $\alpha$-$PbO_2$-type $TiO_2$. *Phys. Status Solidi RRL* **2014**, *8*, 822−826.
(40) Pan, H.; Qiu, X.; Ivanov, I. N.; Meyer, H. M.; Wang, W.; Zhu, W.; Paranthaman, M. P.; Zhang, Z.; Eres, G.; Gu, B. Fabrication and characterization of brookite-rich, visible light-active $TiO_2$ films for water splitting. *Appl. Catal., B* **2009**, *93*, 90−95.
(41) Yang, D.; Liu, H.; Zheng, Z.; Yuan, Y.; Zhao, J. C.; Waclawik, E. R.; Ke, X.; Zhu, H. An Efficient Photocatalyst Structure: $TiO_2$(B) Nanofibers with a Shell of Anatase Nanocrystals. *J. Am. Chem. Soc.* **2009**, *131*, 17885−17893 (PMID: 19911792).
(42) Jiao, Y.; Chen, F.; Zhao, B.; Yang, H.; Zhang, J. Anatase grain loaded brookite nanoflower hybrid with superior photocatalytic activity for organic degradation. *Colloids Surf., A* **2012**, *402*, 66−71.
(43) Lee, H. U.; Lee, Y.-C.; Lee, S. C.; Park, S. Y.; Son, B.; Lee, J. W.; Lim, C.-H.; Choi, C.-J.; Choi, M.-H.; Lee, S. Y.; Oh, Y.-K.; Lee, J. Visible-light-responsive bicrystalline (anatase/brookite) nanoporous nitrogen-doped $TiO_2$ photocatalysts by plasma treatment. *Chem. Eng. J.* **2014**, *254*, 268−275.
(44) Zhu, S.-C.; Xie, S.-H.; Liu, Z.-P. Design and Observation of Biphase $TiO_2$ Crystal with Perfect Junction. *J. Phys. Chem. Lett.* **2014**, *5*, 3162−3168.
(45) Armstrong, A.; Armstrong, G.; Canales, J.; García, R.; Bruce, P. Lithium-Ion Intercalation into $TiO_2$-B Nanowires. *Adv. Mater.* **2005**, *17*, 862−865.
(46) Morgan, B. J.; Madden, P. A. Lithium intercalation into $TiO_2$(B): A comparison of LDA, GGA, and GGA+U density functional calculations. *Phys. Rev. B* **2012**, *86*, No. 035147.
(47) Melot, B. C.; Tarascon, J.-M. Design and Preparation of Materials for Advanced Electrochemical Storage. *Acc. Chem. Res.* **2013**, *46*, 1226−1238 (PMID: 23282038).
(48) Subramanian, V.; Karki, A.; Gnanasekar, K.; Eddy, F. P.; Rambabu, B. Nanocrystalline $TiO_2$ (anatase) for Li-ion batteries. *J. Power Sources* **2006**, *159*, 186−192.
(49) Pfanzelt, M.; Kubiak, P.; Fleischhammer, M.; Wohlfahrt-Mehrens, M. $TiO_2$ rutile—An alternative anode material for safe lithium-ion batteries. *J. Power Sources* **2011**, *196*, 6815−6821.
(50) Zhang, S. B.; Wei, S. H.; Zunger, A. Intrinsic *n*-type versus *p*-type doping asymmetry and the defect physics of ZnO. *Phys. Rev. B* **2001**, *63*, No. 075205.
(51) Walsh, A.; Catlow, C. R. A.; Miskufova, M.; Sokol, A. A. Electron and hole stability in GaN and ZnO. *J. Phys.: Condens. Matter* **2011**, *23*, No. 334217.
(52) Walsh, A.; Buckeridge, J.; Catlow, C. R. A.; Jackson, A. J.; Keal, T. W.; Miskufova, M.; Sherwood, P.; Shevlin, S. A.; Watkins, M. B.; Woodley, S. M.; Sokol, A. A. Limits to Doping of Wide Band Gap Semiconductors. *Chem. Mater.* **2013**, *25*, 2924−2926.
(53) Bhachu, D. S.; Sathasivam, S.; Sankar, G.; Scanlon, D. O.; Cibin, G.; Carmalt, C. J.; Parkin, I. P.; Watson, G. W.; Bawaked, S. M.; Obaid, A. Y.; Al-Thabaiti, S.; Basahel, S. N. Solution Processing Route to Multifunctional Titania Thin Films: Highly Conductive and Photcatalytically Active Nb:$TiO_2$. *Adv. Funct. Mater.* **2014**, *24*, 5075−5085.
(54) Kafizas, A.; Noor, N.; Carmichael, P.; Scanlon, D. O.; Carmalt, C. J.; Parkin, I. P. Combinatorial Atmospheric Pressure Chemical Vapor Deposition of F:$TiO_2$; the Relationship between Photocatalysis and Transparent Conducting Oxide Properties. *Adv. Funct. Mater.* **2014**, *24*, 1758−1771.
(55) Orita, M.; Ohta, H.; Hirano, M.; Hosono, H. Deep-ultraviolet transparent conductive $\beta$-$Ga_2O_3$ thin films. *Appl. Phys. Lett.* **2000**, *77*, 4166−4168.
(56) Henrich, V. E.; Cox, P. A. *The surface science of metal oxides*; Cambridge University Press: New York, 1996.
(57) Linsebigler, A. L.; Lu, G.; Yates, J. T. Photocatalysis on $TiO_2$ Surfaces: Principles, Mechanisms, and Selected Results. *Chem. Rev.* **1995**, *95*, 735−758.


DOI: 10.1021/acs.chemmater.5b00230
*Chem. Mater.* 2015, 27, 3844−3851

(58) Yang, H. G.; Sun, C. H.; Qiao, S. Z.; Zou, J.; Liu, G.; Smith, S. C.; Cheng, H. M.; Lu, G. Q. Anatase $TiO_2$ single crystals with a large percentage of reactive facets. *Nature* **2008**, *453*, 638−641.
(59) Lin, H.; Li, L.; Zhao, M.; Huang, X.; Chen, X.; Li, G.; Yu, R. Synthesis of High-Quality Brookite $TiO_2$ Single-Crystalline Nanosheets with Specific Facets Exposed: Tuning Catalysts from Inert to Highly Reactive. *J. Am. Chem. Soc.* **2012**, *134*, 8328−8331 (PMID: 22559221).
(60) Yin, W.-J.; Tang, H.; Wei, S.-H.; Al-Jassim, M. M.; Turner, J.; Yan, Y. Band structure engineering of semiconductors for enhanced photoelectrochemical water splitting: The case of $_2$. *Phys. Rev. B* **2010**, *82*, No. 045106.
(61) Deák, P.; Aradi, B.; Frauenheim, T. Quantitative theory of the oxygen vacancy and carrier self-trapping in bulk $TiO_2$. *Phys. Rev. B* **2012**, *86*, No. 195206.
(62) Deák, P.; Kullgren, J.; Frauenheim, T. Polarons and oxygen vacancies at the surface of anatase $TiO_2$. *Phys. Status Solidi RRL* **2014**, *8*, 583−586.
(63) Luttrell, T.; Halpegamage, S.; Tao, J.; Kramer, A.; Sutter, E.; Batzill, M. Why is anatase a better photocatalyst than rutile?—Model studies on epitaxial $TiO_2$ films. *Sci. Rep.* **2014**, *4*, No. 4043.
(64) *ChemShell, a Computational Chemistry Shell*, http://www.chemshell.org, 1999.
(65) Sherwood, P.; de Vries, A. H.; Guest, M. F.; Schreckenbach, G.; Catlow, C. R. A.; French, S. A.; Sokol, A. A.; Bromley, S. T.; Thiel, W.; Turner, A. J.; Billeter, S.; Terstegen, F.; Thiel, S.; Kendrick, J.; Rogers, S. C.; Casci, J.; Watson, M.; King, F.; Karlsen, E.; Sjøvoll, M.; Fahmi, A.; Schäfer, A.; Lennartz, C. QUASI: A general purpose implementation of the QM/MM approach and its application to problems in catalysis. *J. Mol. Struct. (THEOCHEM)* **2003**, *632*, 1−28.
(66) Dick, B. G.; Overhauser, A. W. Theory of the Dielectric Constants of Alkali Halide Crystals. *Phys. Rev.* **1958**, *112*, 90−103.
(67) Sokol, A. A.; Bromley, S. T.; French, S. A.; Catlow, C. R. A.; Sherwood, P. Hybrid QM/MM embedding approach for the treatment of localized surface states in ionic materials. *Int. J. Quantum Chem.* **2004**, *99*, 695−712.
(68) Sokol, A. A.; French, S. A.; Bromley, S. T.; Catlow, C. R. A.; van Dam, H. J. J.; Sherwood, P. Point defects in ZnO. *Faraday Discuss.* **2007**, *134*, 267−282.
(69) Dutta, G.; Sokol, A. A.; Catlow, C. R. A.; Keal, T. W.; Sherwood, P. Activation of Carbon Dioxide over Zinc Oxide by Localised Electrons. *ChemPhysChem* **2012**, *13*, 3453−3456.
(70) Buckeridge, J.; Bromley, S. T.; Walsh, A.; Woodley, S. M.; Catlow, C. R. A.; Sokol, A. A. One-dimensional embedded cluster approach to modeling CdS nanowires. *J. Chem. Phys.* **2013**, *139*, No. 124101.
(71) Butler, K. T.; Buckeridge, J.; Catlow, C. R. A.; Walsh, A. Crystal electron binding energy and surface work function control of tin dioxide. *Phys. Rev. B* **2014**, *89*, No. 115320.
(72) Buckeridge, J.; Catlow, C. R. A.; Scanlon, D. O.; Keal, T. W.; Sherwood, P.; Miskufova, M.; Walsh, A.; Woodley, S. M.; Sokol, A. A. Determination of the Nitrogen Vacancy as a Shallow Compensating Center in GaN Doped with Divalent Metals. *Phys. Rev. Lett.* **2015**, *114*, No. 016405.
(73) Guest, M. F.; Bush, I. J.; van Dam, H. J. J.; Sherwood, P.; Thomas, J. M. H.; van Lenthe, J. H.; Havenith, R. W. A.; Kendrick, J. The GAMESS-UK electronic structure package: algorithms, developments and applications. *Mol. Phys.* **2005**, *103*, 719−747.
(74) Bergner, A.; Dolg, M.; Küchle, W.; Stoll, H.; Preuß, H. Ab initio energy-adjusted pseudopotentials for elements of groups 13−17. *Mol. Phys.* **1993**, *80*, 1431−1441.
(75) Weigend, F.; Ahlrichs, R. Balanced basis sets of split valence, triple zeta valence and quadruple zeta valence quality for H to Rn: Design and assessment of accuracy. *Phys. Chem. Chem. Phys.* **2005**, *7*, 3297−3305.
(76) Zhao, Y.; Lynch, B. J.; Truhlar, D. G. Development and Assessment of a New Hybrid Density Functional Model for Thermochemical Kinetics. *J. Phys. Chem. A* **2004**, *108*, 2715−2719.
(77) Gale, J. D.; Rohl, A. L. The General Utility Lattice Program (GULP). *Mol. Simul.* **2003**, *29*, 291−341.
(78) Born, M., Huang, K. *Dynamical theory of crystal lattices*; Oxford University Press: Oxford, MA, USA, 1956.
(79) Krukau, A. V.; Vydrov, O. A.; Izmaylov, A. F.; Scuseria, G. E. Influence of the exchange screening parameter on the performance of screened hybrid functionals. *J. Chem. Phys.* **2006**, *125*, No. 224106.
(80) Kresse, G.; Hafner, J. *Ab initio* molecular dynamics for liquid metals. *Phys. Rev. B* **1993**, *47*, 558−561.
(81) Kresse, G.; Hafner, J. *Ab initio* molecular-dynamics simulation of the liquid-metal-amorphous-semiconductor transition in germanium. *Phys. Rev. B* **1994**, *49*, 14251−14269.
(82) Kresse, G.; Furthmüller, J. Efficiency of *ab-initio* total energy calculations for metals and semiconductors using a plane-wave basis set. *Comput. Mater. Sci.* **1996**, *6*, 15−50.
(83) Kresse, G.; Furthmüller, J. Efficient iterative schemes for *ab initio* total-energy calculations using a plane-wave basis set. *Phys. Rev. B* **1996**, *54*, 11169−11186.
(84) Blöchl, P. E. Projector augmented-wave method. *Phys. Rev. B* **1994**, *50*, 17953−17979.


DOI: 10.1021/acs.chemmater.5b00230
*Chem. Mater.* 2015, 27, 3844−3851